Synthesis, Structural, Thermal, and Electronic Properties of Palmierite-Related Double Molybdate α-Cs$_2$Pb(MoO$_4$)$_2$

Sergey F. Solodovnikov,[†,‡] Victor V. Atuchin,[*,§,∥,⊥,#,▲] Zoya A. Solodovnikova,[†] Oleg Y. Khyzhun,[∇] Mykola I. Danylenko,[∇] Denis P. Pishchur,[○] Pavel E. Plyusnin,[‡,◆] Alexey M. Pugachev,[%] Tatiana A. Gavrilova,[@] Alexander P. Yelisseyev,[□] Ali H. Reshak,[■,◇] Zeyad A. Alahmed,[◆] and Nadir F. Habubi[●]

[†]Laboratory of Crystal Chemistry, [○]Laboratory of Physical Chemistry of Condensed Matter, and [◆]Laboratory of Rare Platinum Group Metals, Nikolaev Institute of Inorganic Chemistry, SB RAS, Novosibirsk 630090, Russia

[‡]Department of Natural Sciences and [⊥]Laboratory of Semiconductor and Dielectric Materials, Novosibirsk State University, Novosibirsk 630090, Russia

[§]Laboratory of Optical Materials and Structures and [@]Laboratory of Nanodiagnostics and Nanolithography, Institute of Semiconductor Physics, SB RAS, Novosibirsk 630090, Russia

[∥]Functional Electronics Laboratory, Tomsk State University, Tomsk 634050, Russia

[▲]Laboratory of Single Crystal Growth, South Ural State University, Chelyabinsk 454080, Russia

[#]Institute of Chemistry, Tyumen State University, Tyumen 525003, Russia

[∇]Frantsevich Institute for Problems of Materials Science, National Academy of Sciences of Ukraine, 3 Krzhyzhanivsky Street, Kyiv UA-03142, Ukraine

[%]Laboratory of Condensed Matter Spectroscopy, Institute of Automation and Electrometry, SB RAS, Novosibirsk 90, 630090, Russia

[□]Laboratory of High Pressure Minerals and Diamond Deposits, Institute of Geology and Mineralogy, SB RAS, Novosibirsk 630090, Russia

[■]New Technologies - Research Centre, University of West Bohemia, Univerzitni 8, 306 14 Pilsen, Czech Republic

[◇]School of Material Engineering, University Malaysia Perlis, 01007 Kangar, Perlis, Malaysia

[◆]Department of Physics and Astronomy, College of Science, King Saud University, P.O. Box 2455, Riyadh 11451, Saudi Arabia

[●]Physics Department, Education Faculty, University of Al-Mustansiriyah, Baghdad, Iraq

S *Supporting Information*

ABSTRACT: Cs$_2$Pb(MoO$_4$)$_2$ crystals were prepared by crystallization from their own melt, and the crystal structure has been studied in detail. At 296 K, the molybdate crystallizes in the low-temperature α-form and has a monoclinic palmierite-related superstructure (space group $C2/m$, a = 2.13755(13) nm, b = 1.23123(8) nm, c = 1.68024(10) nm, β = 115.037(2)°, Z = 16) possessing the largest unit cell volume, 4.0066(4) nm^3, among lead-containing palmierites. The compound undergoes a distortive phase transition at 635 K and incongruently melts at 943 K. The electronic structure of α-Cs$_2$Pb(MoO$_4$)$_2$ was explored by using X-ray emission spectroscopy (XES) and X-ray photoelectron spectroscopy methods. For α-Cs$_2$Pb(MoO$_4$)$_2$, the photoelectron

α–Cs₂Pb(MoO₄)₂

core-level and valence-band spectra and the XES band representing the energy distribution of Mo 4d and O 2p states were recorded. Our results allow one to conclude that the Mo 4d and O 2p states contribute mainly to the central part and at the top of the valence band, respectively, with also significant contributions throughout the whole valence-band region of the molybdate under consideration.
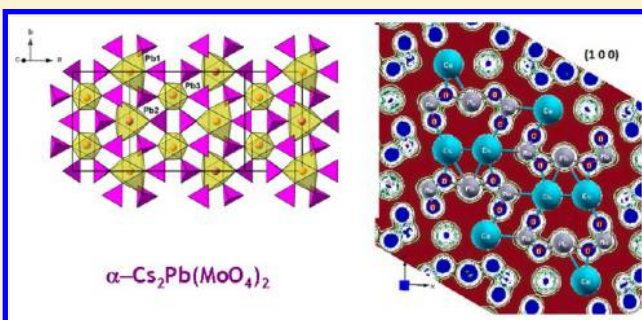
1. INTRODUCTION

A number of double molybdates and tungstates of alkaline and divalent metals have attracted much attention from scientific and technological points of view due to their potential applications as luminescent, ion-conducting, ferroelastic, and scintillating materials.[1−8] Among these compounds, double

molybdates with general formula A_2Pb(MoO$_4$)$_2$ (A = K, Rb, Cs) are of particular interest as members of a large structural family of palmierite K$_2$Pb(SO$_4$)$_2$ (space group $R\bar{3}m$; a = 0.549 nm;

$c = 2.083$ nm) with general crystal chemical formula $M1^{[6+6]}$-$M2^{[10]}_2(XO_4)_2$.[9−12] The most known representative crystals of the family are ferroelastics $Pb_3(XO_4)_2$ (X = P, As, V) with monoclinic structure. It has been found that the ferroelastic transition $R\bar{3}m \rightarrow C2/c$ at 453 K in $Pb_3(PO_4)_2$ is mainly realized through shifts of Pb^{2+} cations and PO_4^{3-} anions from the 3-fold axes.[13,14] Also, the second-order ferroelastic transitions between the palmierite-type trigonal phase and the monoclinic one were observed in $Cs_2Pb(MoO_4)_2$, $Rb_2Pb(MoO_4)_2$, and $K_2Pb(MoO_4)_2$ at 626, 496, and 448 K, respectively.[3,15] The crystals can be prepared by conventional solid state reactions from A_2MoO_4 (A = K, Rb, Cs) and $PbMoO_4$ followed by spontaneous crystallization at slow cooling from their own melts or melts with adding $A_2Mo_2O_7$ fluxes.[15,16] The phase transitions existing in the compounds were attributed to the effect of $6s^2$ lone electron pairs of Pb^{2+}.[11,13] Later, it was shown that the monoclinic structures of α-$A_2Pb(MoO_4)_2$ (A = K[16] and Rb[17]) have a different character of the palmierite structure distortion, as compared to that of α-$Pb_3(PO_4)_2$.

Palmierite-related α-$A_2Pb(MoO_4)_2$ (A = K and Rb) at ambient temperatures have the following cell parameters: $a = 1.0377(6)$ nm, $b = 0.7812(9)$ nm, $c = 2 \times 0.5993(8)$ nm, and $\beta = 115.88(8)°$ for the former[16] and $a = 2.09724(15)$ nm, $b = 1.21261(8)$ nm, $c = 1.61171(10)$ nm, and $\beta = 115.728(13)°$ for the latter.[17] As established in ref 17, the cell parameters of α-$Rb_2Pb(MoO_4)_2$ have a simple relation with α-$K_2Pb(MoO_4)_2$: $a_{RbPb} = -2a_{KPb}$, $b_{RbPb} = 2c_{KPb}$, and $c_{RbPb} = 2b_{KPb}$. This means that the unit cell volume of α-$Rb_2Pb(MoO_4)_2$ is increased 8 times as compared to that of α-$K_2Pb(MoO_4)_2$. The above-mentioned fact indicates a more complex structure of α-$Rb_2Pb(MoO_4)_2$ in comparison with that of α-$K_2Pb(MoO_4)_2$. Furthermore, the isostructurality of α-$K_2Pb(MoO_4)_2$ and α-$Rb_2Pb(MoO_4)_2$ can occur because the α-$K_2Pb(MoO_4)_2$ structure was established within a subcell.[16] It should be mentioned that α-$Rb_2Pb(MoO_4)_2$ possesses the largest cell volume value and the most complex structure among lead-containing palmierites.[17]

To the best of our knowledge, the structural and many other characteristics of α-$Cs_2Pb(MoO_4)_2$ is still unknown. In the present work, to fill the gap, the monophase polycrystalline powder and high-quality single crystals of α-$Cs_2Pb(MoO_4)_2$ have been prepared and their structural characteristics determined in detail. Earlier, in the first-principles band structure calculations and experimental studies of molybdates,[18−24] as well as double molybdates and tungstates,[25−28] it was exhibited that their electronic structures are dominated by significant contributions of the Mo(W) d and O p states over the whole valence-band region. In the present study, besides X-ray photoelectron spectroscopy (XPS), X-ray emission spectroscopy (XES) was implemented to record the XE Mo $L\beta_{2,15}$ and O $K\alpha$ bands yielding the energy distribution of Mo 4d and O 2p states, respectively, for α-$Cs_2Pb(MoO_4)_2$. Then, on a common energy scale, the XE Mo $L\beta_{2,15}$ and O $K\alpha$ bands of α-$Cs_2Pb(MoO_4)_2$ were compared with its valence-band spectrum carried out by XPS. Finally, the α-$Cs_2Pb(MoO_4)_2$ band structure was calculated and compared to the experimental results.

2. METHODOLOGY

2.1. Synthesis. Commercially available Cs_2CO_3 (reagent grade) and MoO_3 and $PbMoO_4$ (both analytical grade) were used as initial materials for solid state synthesis. Cesium molybdate Cs_2MoO_4 was prepared by heat treatment of the stoichiometric mixture of Cs_2CO_3 and MoO_3 at 673, 723, and 823 K for 24, 40, and 60 h, respectively. Double-molybdate $Cs_2Pb(MoO_4)_2$ was prepared from the stoichiometric

mixture of Cs_2MoO_4 and $PbMoO_4$ by annealing at 723 K for 50 h, 773 K for 50 h, 823 K for 50 h, and 873 K for 50 h with intermittent regrinding every day in an agate mortar to yield the sample composition homogeneity. The colorless $Cs_2Pb(MoO_4)_2$ plate-like crystals were obtained by cooling the melt from 973 K to room temperature in a turned-off furnace. The photo of the microcrystals is shown in Figure 1S. *Caution! $PbMoO_4$ and $Cs_2Pb(MoO_4)_2$ are insoluble in water but harmful as dusts if inhaled. Sample preparation and intermittent regrinding of these materials should be performed with protective gloves and glasses under exhaust ventilation.*

2.2. Characterization Methods. The phase purity of the final powder product was verified by X-ray diffraction (XRD) analysis using a DRON SEIFERT RM4 diffractometer (Cu Kα radiation, Ni filter, 2θ range of 5−70°, scanning rate 0.5 deg/min) at room temperature. The differential scanning calorimetry (DSC) measurements were performed by a heat flow measurement method on a Netzsch STA 449 F1 Jupiter thermoanalyzer over the temperature range of 303−1073 K at a heating rate of 10 K/min and a Netzsch DSC 204 F1 Phoenix calorimeter over the temperature range of 293−700 K, heating rate of 6 K/min, in Ar flow of 25 mL/min. The SHG response was determined in the backscattering geometry using the modified Kurtz−Perry method.[29] The SHG signal in the powder sample was excited by nanosecond-pulsed irradiation from a Nd:YAG laser (STA-01-7, Standa) ($\lambda = 1064$ nm, mean power 100 mW, repetition rate 1 kHz). The signal at $\lambda = 532$ nm recorded by a photomultiplier was selected by a collimator and a monochromator MDR-2. The quartz powder sample with known nonlinear optical characteristics was used as a reference.

The particle micromorphology was evaluated by SEM using an LEO 1430 device. The sample handling methods and measurement conditions can be found elsewhere.[30,31] The characteristic particle size and chemical composition were determined from TEM images obtained by a JEM-2100F microscope (JEOL, Japan) operated at 200 kV and supplied with an OXFORD-Inca Energy EDS X-ray microanalysis system. The X-ray diffraction data for single-crystal α-$Cs_2Pb(MoO_4)_2$ structure determination were collected using a Bruker-Nonius X8-Apex CCD area-detector diffractometer ($T = 296(2)$ K, $\lambda = 0.071073$ nm, graphite monochromator, φ scans, scan step of 0.5°). The structure was refined and solved using the SHELX-97 package.[32]

The XPS spectra of α-$Cs_2Pb(MoO_4)_2$ were recorded by a UHV-Analysis-System (SPECS Surface Nano Analysis Co., Germany) equipped with a PHOIBOS 150 analyzer. When measuring the XPS spectra, the base pressure of a sublimation-ion-pumped chamber of the system was below 3×10^{-8} Pa. For spectra excitation, Mg Kα irradiation ($E = 1253.6$ eV) was used. The XPS spectra of α-$Cs_2Pb(MoO_4)_2$ were recorded at a pass energy of 25 eV. The energy scale of the spectrometer was calibrated by setting the Au $4f_{7/2}$ and Cu $2p_{3/2}$ binding energies of reference Au and Cu samples to 84.00 ± 0.05 and 932.66 ± 0.05 eV, respectively, with respect to the Fermi energy, E_F. The energy drift induced by charging effects was accounted for, taking the C 1s (284.6 eV) core level of hydrocarbons, as it was provided for dielectric molybdenum oxides.[19,23,24]

The technique for measurements of the XE Mo $L\beta_{2,15}$ and O $K\alpha$ bands of α-$Cs_2Pb(MoO_4)_2$ was similar to that described elsewhere.[33] Briefly, the fluorescent X-ray emission Mo $L\beta_{2,15}$ band ($L_{III} \rightarrow N_{IV,V}$ transition), which represents mainly the Mo 4d states energy distribution, was carried out with a Johann-type SARF-1 spectrometer taking the $(10\bar{1}1)$ reflecting plane of a quartz crystal with a curvature radius of $R \approx 500$ mm as the dispersing element. The detector was a gas-flow Ar−CH_4 counter. An X-ray tube working at accelerating voltage $U = 6$ kV and anode current $I = 600$ mA was used for band excitation. The XE O $K\alpha$ band related to the K → $L_{II,III}$ transition, giving information regarding energy distribution of the O 2p states, was measured using an RSM-500 spectrometer equipped by a diffraction grating (600 grooves/mm, curvature radius of $R = 6026$ mm). The secondary electron multiplier VEU-6 with CsI photocathode was applied as a detector. A spectrometer electron gun operating at $U = 5$ kV and $I = 2.5$ mA was employed for XE O $K\alpha$ band excitation. The energy resolution ΔE_{min} of the RSM-500 and SARF-1 spectrometers was estimated to be 0.4 and 0.25 eV for recording the XE Mo $L\beta_{2,15}$ and O $K\alpha$ bands, respectively.
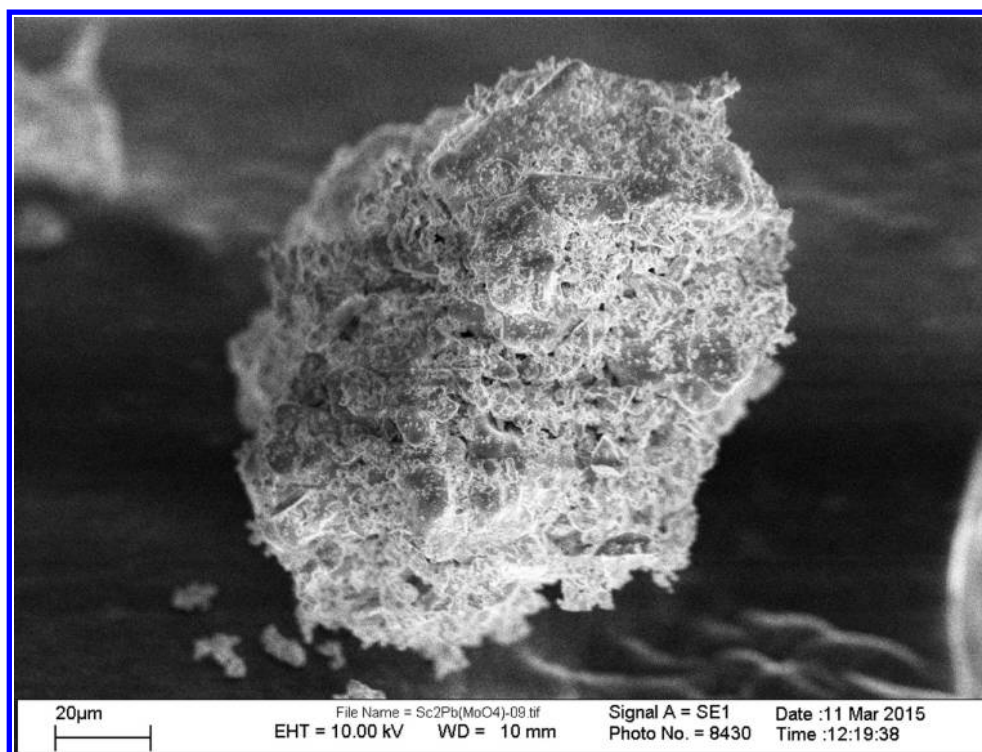
Figure 1. SEM image of a typical $Cs_2Pb(MoO_4)_2$ particle.

2.3. Theoretical Aspect. Further, we made use of density functional theory (DFT) to evaluate the electronic structure, density of states, and electronic charge density distribution of α-$Cs_2Pb(MoO_4)_2$. We used our crystal structure atomic parameters as input data for the theoretical calculation. The all-electrons full potential linear-augmented plane-wave plus the local orbitals (FP-LAPW+lo) method implemented in the WIEN2k code[34] within the generalized gradient approximation (PBE-GGA)[35] were used to reach geometrical relaxation. In Table 1S, the optimized atomic positions are listed and a good relation with the experimental data is evident. From the relaxed geometry, we obtained the ground stated properties using the Becke−Johnson potential (mBJ) modified recently.[36] The projected density of states was obtained by the modified tetrahedron method.[37] The input data required for the density of states calculation are the energy eigenvalues/eigenfunctions obtained from the band-structure calculation. To reach the total energy convergence, the base functions over the interstitial region were expanded up to $R_{MT} \times K_{max} = 7.0$ and for the wave function inside the atomic spheres. The maximal value of l is taken as $l_{max} = 10$, while the charge density was Fourier expanded up to $G_{max} = 12.0\ (au)^{-1}$. The self-consistency was obtained using 400 $\vec{k}$ points over the irreducible Brillouin zone (IBZ). Since the system total energy is stable within 0.00001 Ry, the self-consistent calculations were converged. The calculations of the band structure, density of states, and electronic charge density were performed within 1000 $\vec{k}$ points in the IBZ.

3. RESULTS AND DISCUSSION

3.1. Sample Characterization. The solid state reaction between Cs_2MoO_4 and $PbMoO_4$ leads to the formation of single-phase final white-colored product, $Cs_2Pb(MoO_4)_2$. The typical SEM image recorded from the compound is shown in Figure 1. The powder contains the irregular partly agglomerated particles with characteristic dimensions of 5−15 μm and without any faceting. Besides big particles, the presence of a small-size fraction is evident. As it can be concluded, the shape/size parameters of the microcrystals are inhomogeneous. The noticeable charging effect was detected during measurements,
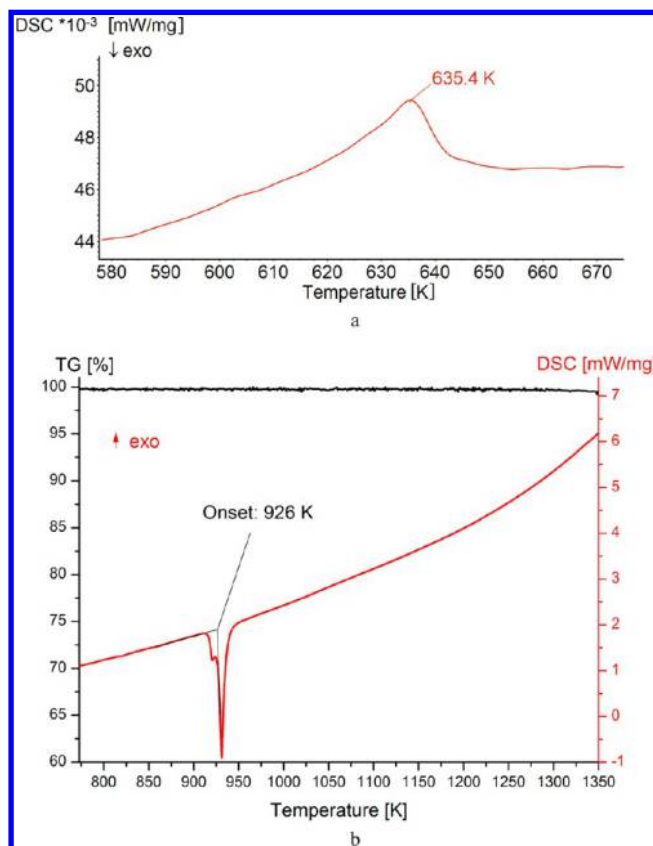

Figure 2. DSC curves of a sintered $Cs_2Pb(MoO_4)_2$ sample: (a) fragment of the DSC curve over the phase transition range; (b) fragment of the DSC curve around the melting point.

and this indicates low conductivity of the particles. TEM results allow for concluding that the $Cs_2Pb(MoO_4)_2$ powder subjected

Table 1. Single-Crystal XRD and Refinement Data for α-Cs$_2$Pb(MoO$_4$)$_2$

|	
fw	792.89
cryst syst, space group	monoclinic, $C2/m$
unit cell params	$a = 2.13755(13)$ nm
	$b = 1.23123(8)$ nm
	$c = 1.68024(10)$ nm
	$\beta = 115.037(2)°$
cell volume, nm^3/Z	4.0066(4)/16
d_{calcd}, g/cm^3	5.258
μ(Mo Kα), mm^{-1}	26.405
cryst dimens, mm	$0.08 \times 0.05 \times 0.04$
theta range for data collection	1.34−36.35°
limiting Miller indices	$-35 \leq h \leq 35$
	$-19 \leq k \leq 20$
	$-18 \leq l \leq 27$
no. of mead reflns	28 027
no. of used reflens $n\ [I > 2\sigma(I)]$	9796 [R(int) = 0.0601]
no. of refined params p	275
extinction coefficient	0.000004(7)
goodness-of-fit $S = [\Sigma w[(F(\exp)^2 - F(\text{calcd})^2]^2/(n - p)]^{1/2}$	0.793
$R(F)$ and $wR(F^2)$ for $I > 2\sigma(I)$	0.0593 and 0.2184
$R(F)$ and $wR(F^2)$ for all refls	0.1281 and 0.2792
extrema of $\Delta\rho(xyz)$, e nm^{-3}	$4.847 \times 10^{-3}/-3.731 \times 10^{-3}$
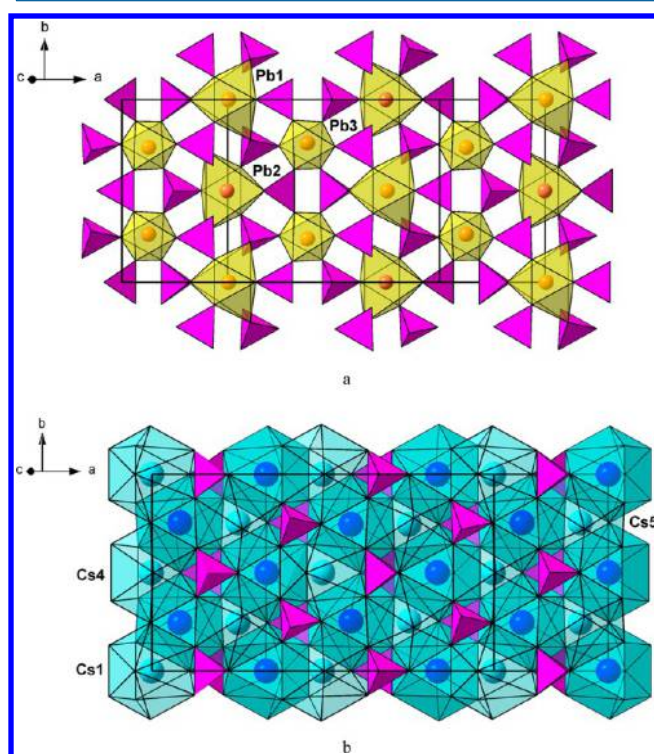
Figure 3. Layers of lead and cesium coordination polyhedra in α-Cs$_2$Pb(MoO$_4$)$_2$ structure in the projection on the (001) plane: (a) layer at the level $z \approx 0.75$; (b) double layer at the level $z \approx 0.5$.

Figure 4. Survey XPS spectrum of α-Cs$_2$Pb(MoO$_4$)$_2$.

to XPS and XES experiments contained particles whose size ranges from 2 to 9 μm. As an example, a TEM image of a typical Cs$_2$Pb(MoO$_4$)$_2$ particle is demonstrated in Figure 2S. Our EDS results (not presented here) reveal the presence of only Cs, Pb, Mo, and O atoms in the particles synthesized in the present work with an average percent atomic composition of 14.65% Cs, 7.81% Pb, 13.25% Mo, and 64.29% O to give the composition Cs$_{1.82}$Pb$_{0.97}$Mo$_{1.65}$O$_8$. These EDS results are found to be consistent with our XPS data.
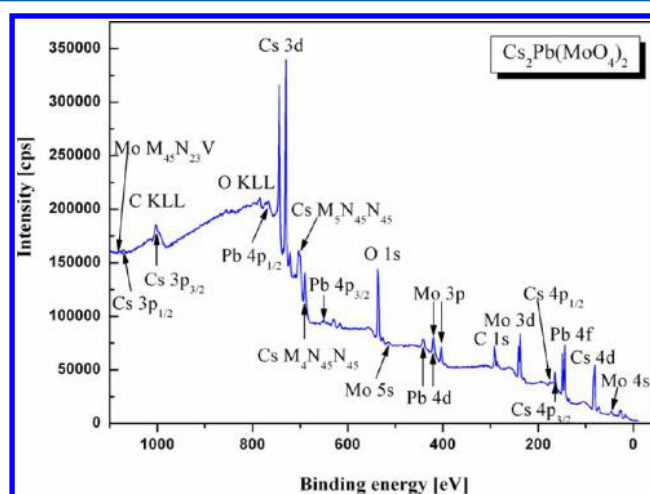
According to the DSC measurements shown in Figure 2, the obtained compound has a second-order phase transition at 635 $\pm$ 2 K (Figure 2a) and melts at 926 $\pm$ 3 K. As to the phase transition, a distortive character was also confirmed by crystal optical observations on a polarizing microscope equipped by a hot stage where a biaxial crystal of Cs$_2$Pb(MoO$_4$)$_2$ was found to become uniaxial above 640 $\pm$ 2 K, which is in agreement with earlier results.[15] The temperatures of the phase transition and melting point agreed well with the earlier reported values.[15,38,39] The products of Cs$_2$Pb(MoO$_4$)$_2$ incongruent melting were found to be Cs$_2$MoO$_4$ and PbMoO$_4$. Testing powder samples of α-Cs$_2$Pb(MoO$_4$)$_2$ at room temperature by the SHG method showed that the phase is characterized by an evidently low SHG level $I_{2\omega}/I_{2\omega}(\text{SiO}_2) = 0.003-0.025$, and therefore, it should be classified as centrosymmetric.

3.2. Crystal Structure. The structure of monoclinic α-Cs$_2$Pb(MoO$_4$)$_2$ was solved by direct methods in the centrosymmetrical space group $C2/m$, which was confirmed with subsequent structure refinement. At the final stage of the refinement,
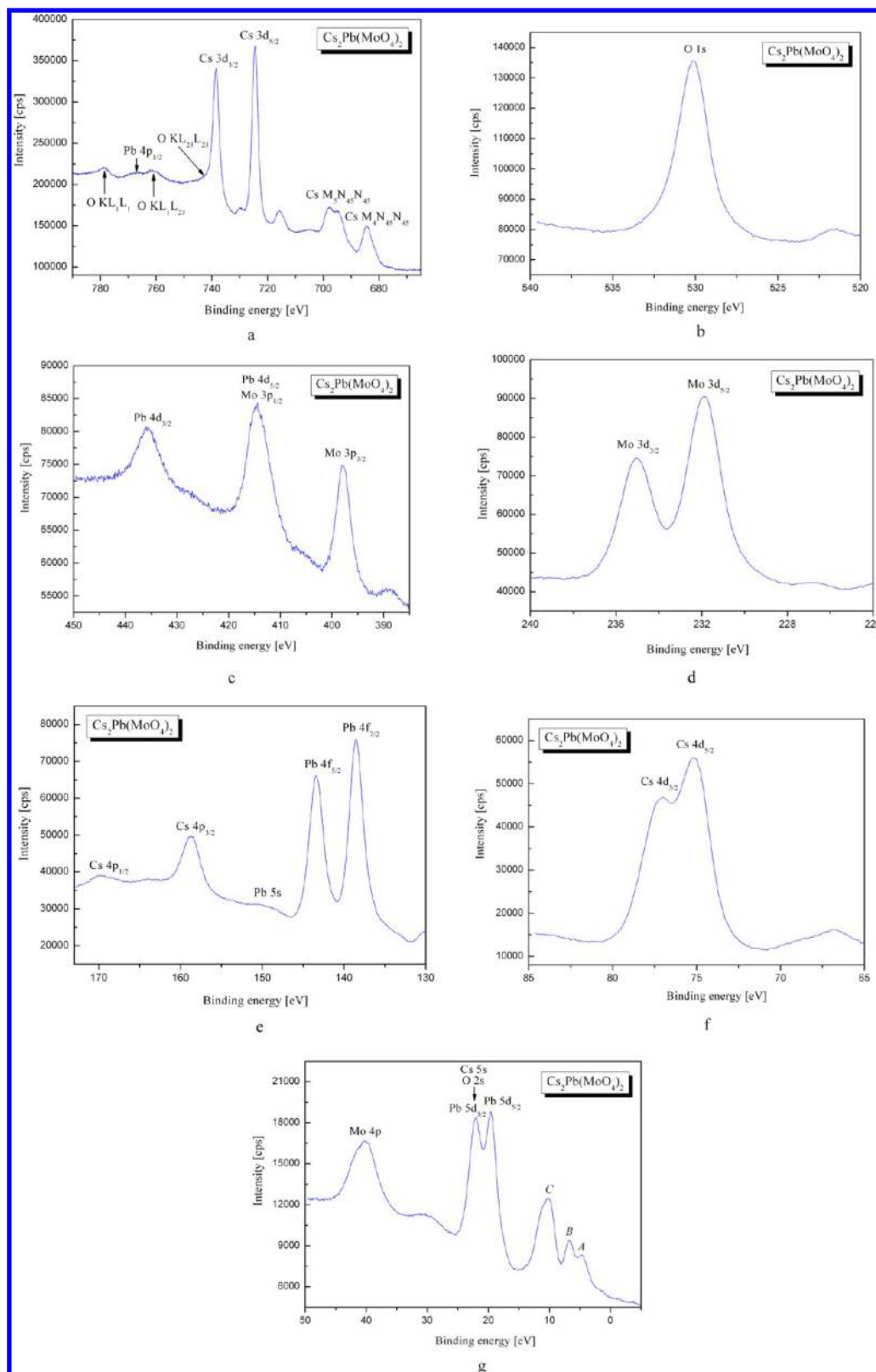
Figure 5. Detailed XPS (a) Cs 3d and Pb 4p$_{1/2}$ core-level spectra and the O KLL and CsMNN Auger lines, (b) O 1s, (c) Pb 4d and Mo 3p, (d) Mo 3d, (e) Pb 4f, Pb 5s, and Cs 4p, and (f) Cs 4d core-level spectra; (g) valence-band spectrum, including upper Pb 5d, Cs 5s, O 2s, and Mo 4p core levels.

a correction for crystal twinning ("tripling") was introduced that led to the refined ratio of the volumes of three crystal twin components as 0.679:0.162(2):0.159(2) at final R = 0.0584. Attempts to refine the structure in space group $C2$ or Cm were unsuccessful and resulted in an unstable refinement with a drastic increase in the R factor. The crystal data and final structure results for α-Cs$_2$Pb(MoO$_4$)$_2$ in space group $C2/m$ are summarized in Table 1. The atomic coordinates and equivalent parameters of

Table 2. Constituent Element Core Levels and Auger Lines Binding Energies (± 0.05 eV) in α-Cs$_2$Pb(MoO$_4$)$_2$

core level, Auger line	binding energy, eV
VB (fine-structure features A, B, and C)	4.75, 6.77, and 10.24
Pb 5d$_{5/2}$	19.65
Pb 5d$_{3/2}$ + O 2s + Cs 5s	22.08
Mo 4p	40.27
Cs 4d$_{5/2}$	75.21
Cs 4d$_{3/2}$	77.03
Pb 4f$_{7/2}$	138.54
Pb 4f$_{5/2}$	143.41
Cs 4p$_{3/2}$	158.76
Cs 4p$_{1/2}$	169.9[a]
Mo 3d$_{5/2}$	231.91
Mo 3d$_{3/2}$	235.03
C 1s	fixed at 284.6 eV
Mo 3p$_{3/2}$	397.89
Mo 3p$_{1/2}$ + Pb 4d$_{5/2}$	414.61
Pb 4d$_{3/2}$	435.79
O 1s	530.14
Pb 4p$_{3/2}$	645.1[a]
Cs M$_4$N$_{45}$N$_{45}$	684.40
Cs M$_5$N$_{45}$N$_{45}$	697.78
Cs 3d$_{5/2}$	724.54
Cs 3d$_{3/2}$ + O KL$_{23}$L$_{23}$	738.52
O KL$_1$L$_{23}$	761.2[a]
O KL$_1$L$_1$	778.7[a]

[a]Uncertainty of the measurements is ± 0.1 eV.

atomic displacements are given in Table 1S, the selected interatomic distances are enumerated in Table 2S. To the best of our knowledge, the lattice parameters reported in Table 1 were determined for the first time. The atomic coordinates, anisotropic displacement parameters, and other crystal structure details, as solved for α-Cs$_2$Pb(MoO$_4$)$_2$, can be obtained from Fachinformationszentrum Karlsruhe, 76344 Eggenstein Leopoldshafen, Germany (E-mail: crysdata@fiz.karlsruhe.de, http://www.fiz-karlsruhe.de/request), depository number CSD 432157.

The α-Cs$_2$Pb(MoO$_4$)$_2$ structure is isotypical to one of α-Rb$_2$Pb(MoO$_4$)$_2$,[17] and both are palmierite superstructures; their unit cell vectors are related to the palmierite ones as $\boldsymbol{a} = 2\boldsymbol{a}_p + 4\boldsymbol{b}_p$, $\boldsymbol{b} = -2\boldsymbol{a}_p$, $\boldsymbol{c} = 2(-\boldsymbol{a}_p - 2\boldsymbol{b}_p + \boldsymbol{c}_p)/3$. According to these relations, the pseudohexagonal palmierite-like subcell parameters for α-Cs$_2$Pb(MoO$_4$)$_2$ are $a_p = 0.6156$ nm, $b_p = 0.6167$ nm, $c_p = 2.2835$ nm, $\alpha_p = 89.95°$, $\beta_p = 90.00°$, and $\gamma_p = 119.94°$. Like in the case of α-Rb$_2$Pb(MoO$_4$)$_2$, the structure of α-Cs$_2$Pb(MoO$_4$)$_2$ is the most complex one among Pb-containing palmierites. Note that the isostructurality of both compounds to α-K$_2$Pb(MoO$_4$)$_2$ is not excluded, though earlier the latter structure was solved in the subcell with one-eighth of the unit cell volume of α-A$_2$Pb(MoO$_4$)$_2$ (A = Rb, Cs).[16] The α-K$_2$Sr(MoO$_4$)$_2$ structure (space group $C2/c$, $a = 1.4318(3)$ nm, $b = 0.59337(12)$ nm, $c = 1.0422(2)$ nm, $\beta = 105.83(3)°$, $Z = 4$) is also a monoclinic palmierite superstructure, but its unit cell vectors are the same as those of α-Pb$_3$(PO$_4$)$_2$:[14] $\boldsymbol{a}_{KSr} = (-2\boldsymbol{a}_p - \boldsymbol{b}_p + 2\boldsymbol{c}_p)/3$; $\boldsymbol{b}_{KSr} = -\boldsymbol{b}_p$; $\boldsymbol{c}_{KSr} = 2\boldsymbol{a}_p + \boldsymbol{b}_p$.[4]

The α-Cs$_2$Pb(MoO$_4$)$_2$ structure is ordered, 10 of 15 independent metal atoms (2Pb, 4Cs, 4Mo) and 8 of 20 oxygen atoms are located on mirror planes, and the other atoms are in general positions. The Mo atoms are coordinated tetrahedrally with Mo–O distances of 0.164(2)–0.187(3) nm. The Pb(1) and
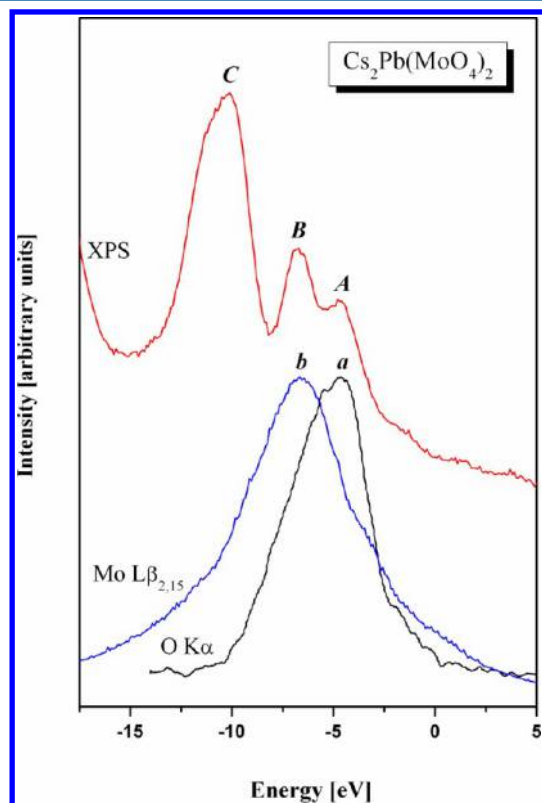
Pb(2) atoms are shifted from the centers of their coordination polyhedra to the most wide base faces, whereas the Pb(3) locates in an elongated octahedron (Figure 3a); this leads to a considerable irregularity of the lead coordinations. Within the sphere of radius 0.32 nm, the Pb(1), Pb(2), and Pb(3) atoms have CN 4 + 2, 4 + 2, and 6, respectively, with the total range of Pb–O distances of 0.235(2)–0.309(3) nm. Note, in the structure of α-Rb$_2$Pb(MoO$_4$)$_2$,[17] the analogous lead atoms have CN 5 + 1, 6, and 5 + 3, respectively, which may be connected with a less covalent character of Pb–O bonds in the rubidium analog compared to the cesium-containing compound with more ionic Cs–O bonds. Cesium cations have a rather regular oxygen environment with CN 10, and Cs–O 0.282(5)–0.360(2) nm.

Like in a palmierite, the α-Cs$_2$Pb(MoO$_4$)$_2$ structure consists of two kinds of layers. The first one is composed of the lead polyhedra and MoO$_4$ tetrahedra sharing common vertices (Figure 4a); these layers are interleaved by double layers of cesium polyhedra (Figure 3b). The pseudotrigonal character of α-Cs$_2$Pb(MoO$_4$)$_2$ structure is readily revealed in the (001) projections (Figure 3) with the visible deviations from the 3-fold symmetry resulting mainly from the MoO$_4$ tetrahedra shifts and rotations with cooperative changing environments of the lead atoms. This makes α-A$_2$Pb(MoO$_4$)$_2$ (A = Rb, Cs) differ from other monoclinic lead-containing palmierites Pb$_3$(XO$_4$)$_2$ (X = P, V, As), where distortions of the palmierite-type structure are mainly caused by shifts of the lead atoms from their initial positions at 3-fold axes with parallel changes in their coordinations [7, 9, 10].

3.3. Electronic Structure Measurements. In Figure 4, the survey XPS spectrum of α-Cs$_2$Pb(MoO$_4$)$_2$ is shown. It is obvious that all spectral features, excluding the carbon 1s level and C KLL Auger line, originated from surface-adsorbed adventitious hydrocarbons, can be attributed to the constituent element core levels or Auger lines. As can be seen from Figure 4, the relative intensity of the C 1s core-level line, as recorded from the α-Cs$_2$Pb(MoO$_4$)$_2$ surface, was rather weak. The relative constituent element ratio was estimated using the detailed spectra of the Cs 3d, Pb 4f$_{7/2}$, Mo 3d$_{5/2}$, and O 1s core-level lines and the tabulated atomic sensitivity factors (ASF).[40] In the case of ignoring the presence of adsorbed carbon-containing species at the sample surface, the resulting composition Cs:Pb:Mo:O = 0.158:0.074:0.151:0.617 is in reasonable agreement with the nominal composition of Cs:Pb:Mo:O = 0.154:0.077:0.154:0.615 for this compound. If we take into consideration the above species, the resulting composition Cs:Pb:Mo:O:C is as follows: 0.133:0.062:0.127:0.519:0.159. However, the presence of the carbon-containing adsorbates does not influence noticeably the binding energies determined in the present work for the constituting atoms of α-Cs$_2$Pb(MoO$_4$)$_2$ as well as the energy distribution of the electronic states over the valence band.

The superposition of the Cs 3d core level and the Auger O KLL line in α-Cs$_2$Pb(MoO$_4$)$_2$ is shown in Figure 5a. Nevertheless, as it can be observed from Figure 5a, the relative intensity of the O KL$_{23}$L$_{23}$ line is rather low, as compared to that of the Cs 3d$_{3/2}$ line; therefore, the binding energy values of the Cs 3d$_{3/2}$ and Cs 3d$_{5/2}$ levels can be determined precisely. Further, the XPS Pb 4p$_{1/2}$ core-level spectrum superimposes the O KL$_1$L$_{23}$ line (Figure 5a). The O 1s core-level spectrum of α-Cs$_2$Pb(MoO$_4$)$_2$ is presented in Figure 5b. It is apparent that the O 1s core-level shape is symmetrical and narrow, which indicates the absence of the OH groups adsorbed at the α-Cs$_2$Pb(MoO$_4$)$_2$ surface. This fact allows us to state that α-Cs$_2$Pb(MoO$_4$)$_2$ is a rather stable compound with respect to the hydration in air. The Pb 4d$_{5/2}$ and

Mo $3p_{1/2}$ spectra superimpose each other in α-$Cs_2Pb(MoO_4)_2$, as it is evidenced from Figure 5c. Further, the Mo 3d, Cs 4p, Pb 4f, and Cs 4d spin−orbit doublets are presented in Figure 5d−f. A set of element core levels with several superpositions is detected at comparatively low BE values, as shown in Figure 5g, where the upper XPS Mo 4p, Pb 5d, Cs 5s, and O 2s core-level spectra of α-$Cs_2Pb(MoO_4)_2$ are shown together with the XPS valence-band spectrum. As can be seen in Figure 5g, three fine-structure features, namely, A, B, and C, are detected on the valence-band spectrum, which is formed by superposition of the valence electronic states associated with the elements constituting α-$Cs_2Pb(MoO_4)_2$ (at BE < 12 eV). The BE values of the constituent element core levels and Auger lines detected by the XPS measurements of α-$Cs_2Pb(MoO_4)_2$ are summarized in Table 2.

Regarding the occupation of the electronic states associated with Mo and O atoms in the energy region corresponding to the valence-band region of α-$Cs_2Pb(MoO_4)_2$, a comparison of the XPS valence-band spectrum and the XE Mo $L\beta_{2,15}$ and O Kα bands of α-$Cs_2Pb(MoO_4)_2$ is presented in Figure 6. The algorithm of matching the above-mentioned spectra on a common energy scale is the same as applied successfully in a recent study of Pb_2MoO_5.[41] Unfortunately, the available facilities do not allow carrying out recording of the X-ray emission bands representing the energy distribution of the valence states associated with Cs and Pb atoms. The results plotted in Figure 6 indicate that in α-$Cs_2Pb(MoO_4)_2$ the dominant contributions of the Mo 4d and O 2p states appear in the central portion and near the valence-band top, respectively, with contributions of the mentioned states in other portions of the valence band of the studied compound. These results show that the electronic structure of α-$Cs_2Pb(MoO_4)_2$ differs from the electronic structure of molybdates $MMoO_4$ (M = Mg, Ca, Ni, Zn, Cd, Ba, Pb, Sr)[42−47] as well as of MWO_4 tungstates (M = Ca, Cu, Zn, Cr, Cd, Pb),[46−55] which indicate that in those materials the valence Mo(W) d and O p states contribute significantly in the lower and upper portions of the valence band, respectively. The latter statement is characteristic for the electronic structures of β-Rb-Nd(MoO_4)_2[28] and α-KY(WO_4)_2.[25] As one can see from Figure 6, a comparison of the XES and XPS spectra of α-$Cs_2Pb(MoO_4)_2$ reveals that the maximum of the XE O Kα band coincides with feature A in the XPS valence-band spectrum while the maximum b of the XE Mo $L\beta_{2,15}$ band with the fine peculiarity B of the XPS valence-band spectrum. It should be mentioned that the maximum C of the XPS valence-band spectrum of α-$Cs_2Pb(MoO_4)_2$ should be formed by the valence states contributions associated with Cs and/or Pb atoms. However, at present, we are not able to study those electronic states, as already mentioned above.

3.4. Electronic Band Structure, Density of States, and Electronic Charge Density Distribution. It was reported that for Pb^{2+}-containing materials, neglecting the spin−orbit coupling (SOC) introduces an error of ∼0.5 eV in the calculated energy gap[56,57] due to the incorrect Pb-6p orbitals placement, which form the conduction band minimum (CBM). Therefore, due to the presence of the heavy atom Pb in α-$Cs_2Pb(MoO_4)_2$, in the
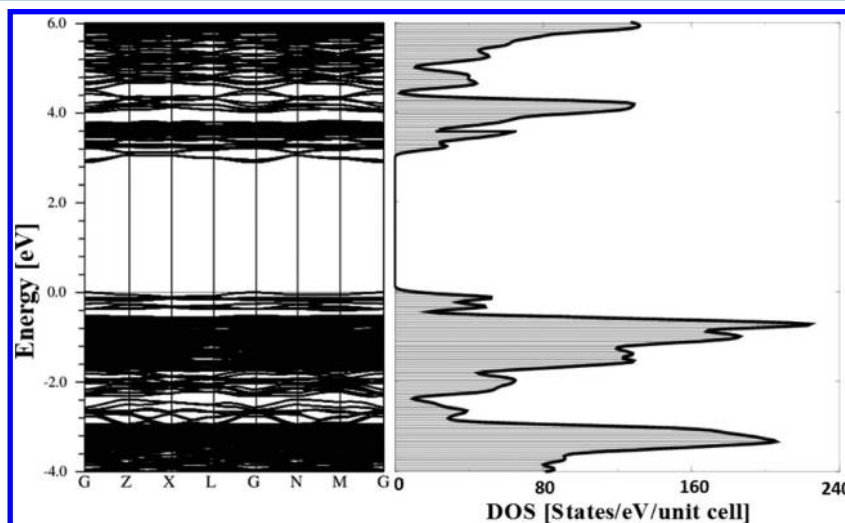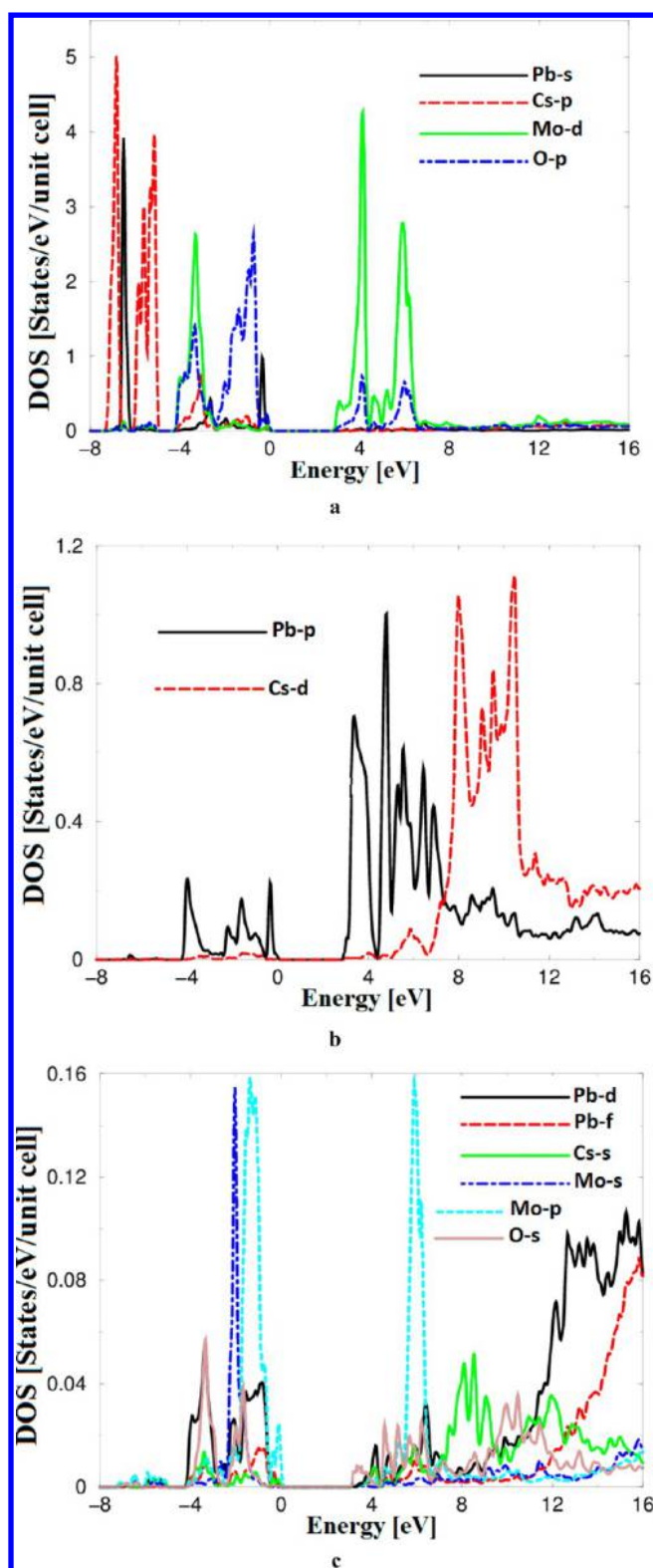

Figure 6. Comparison of the X-ray emission Mo $L\beta_{2,15}$ and O Kα bands as well as the XPS valence-band spectrum of α-$Cs_2Pb(MoO_4)_2$ on a common energy scale.

Figure 7. Calculated electronic band structure and density of states of α-$Cs_2Pb(MoO_4)_2$.

Figure 8. (a−c) Calculated projected density of states of α-Cs$_2$Pb-(MoO$_4$)$_2$.

electronic structure investigation, the SOC effect should be accounted for. Thus, the measured energy band gap is accurately reproduced by combining spin−orbit effects and mBJ. The band structure and total density of states calculated using mBJ+SOC are illustrated in Figure 7. The electronic band structure reveals that α-Cs$_2$Pb(MoO$_4$)$_2$ possesses a direct band gap

($\Gamma_{VBM} - \Gamma_{CBM}$) of about 2.84 eV in close agreement with that estimated from the short cut edge measurements (2.85 eV). It was found that the mBJ+SOC success is in bringing the calculated energy gap close to the measured ones. The associated total density of states accurately reproduce the energy band gap. Furthermore, the project densities of states of α-Cs$_2$Pb(MoO$_4$)$_2$ are shown in Figure 8a−c. It is clear that the valence-band maximum (VBM) is governed by O-2p and Pb-6s orbitals with a small contribution from Mo-4p and Pb-6p orbitals, while the CBM is mainly derived from Pb-6p; therefore, the Pb atoms play a decisive role in the energy band gap determination. The projected density of states reveals that a strong/weak hybridization exists between Pb-s and Cs-p, Pb-s and O-p states, as well as in Cs-p hybridized with Mo-d and O-p states, Pb-d with O-s and Mo-p, and Pb-f with Cs-s states. The hybridization may lead to covalent bond formation.

The calculated projected density of states helps to reveal the bond nature; in the energy region expanding from −8.0 eV to E_F, the total electron number for each orbital can be obtained. It was found that the Cs-6s orbital possesses 5.0 electrons (e), Pb-6s orbital 4.0 e, Mo-d orbital 3.0 e, O-2p orbital 2.8 e, Pb-6p orbital 0.3 e, Mo-5s orbital 0.15 e, Mo-4p orbital 0.16 e, Pb-d orbital 0.06 e, Pb-4f orbital 0.04 e, and O-2s orbital 0.06 e. Therefore, some electrons are transferred from Pb, Cs, Mo, and O atoms into valence bands, and they contribute to the interactions between Pb, Cs, Mo, and O atoms. It should be emphasized that the electronegativity differences play the major role in forming the bonds: the bigger the electronegativity differences are the higher the ionic nature is. The electronegativity of Mo, Pb, O, and Cs, being 2.16, 2.33, 3.48, and 0.79, respectively, is shown with the Pauling scale. Thus, each of Mo and Pb atoms has its tetrahedral and octahedral coordination with O atoms, respectively. To confirm this observation, the valence electronic charge density of α-Cs$_2$Pb(MoO$_4$)$_2$ in two different crystallographic planes was investigated. The (100) plane in which Pb, Cs, Mo, and O atoms are shown is illustrated in Figure 9. It is clear that Mo and Pb atoms form their strong covalent bonding with O atoms, while Cs atoms exhibit ionic bonding. Due to the substantial difference in electronegativity between Pb and O atoms (Figure 9b) and Mo and O atoms (Figure 9c), a charge transfer occurs toward O atoms, as shown by the blue uniform spheres surrounding the O atoms, indicating the maximum charge accumulated according to the thermoscale. Further, for the bonding anisotropy exploration, we calculated the valence electronic charge density in the (1 0 1) plane (Figure 9d), which confirms the tetrahedral and octahedral coordination of Mo−O and Pb−O atoms.

4. CONCLUSIONS

In this work, we prepared powder and single-crystal samples and studied the crystal and electronic structure of α-Cs$_2$Pb(MoO$_4$)$_2$. The phase undergoes a second-order phase transition at 635 $\pm$ 2 K to the palmierite-type modification. The single-crystal XRD study indicates that α-Cs$_2$Pb(MoO$_4$)$_2$ crystallizes in the space group C2/m with unit cell parameters a = 2.13755(13) nm, b = 1.23123(8) nm, c = 1.68024(10) nm, and β = 115.037(2)° (Z = 16). α-Cs$_2$Pb(MoO$_4$)$_2$ and isotypical α-Rb$_2$Pb(MoO$_4$)$_2$ are complicated palmierite superstructures; their unit cells are related to the palmierite ones as $\boldsymbol{a} = 2\boldsymbol{a}_p + 4\boldsymbol{b}_p$, $\boldsymbol{b} = -2\boldsymbol{a}_p$, $\boldsymbol{c} = 2(-\boldsymbol{a}_p - 2\boldsymbol{b}_p + \boldsymbol{c}_p)/3$. Deviations from the trigonal symmetry of palmierite are mainly caused by shifts and rotations of MoO$_4$ tetrahedra with cooperative changing environments of the lead atoms. This differs α-A$_2$Pb(MoO$_4$)$_2$ (A = Cs, Rb) from
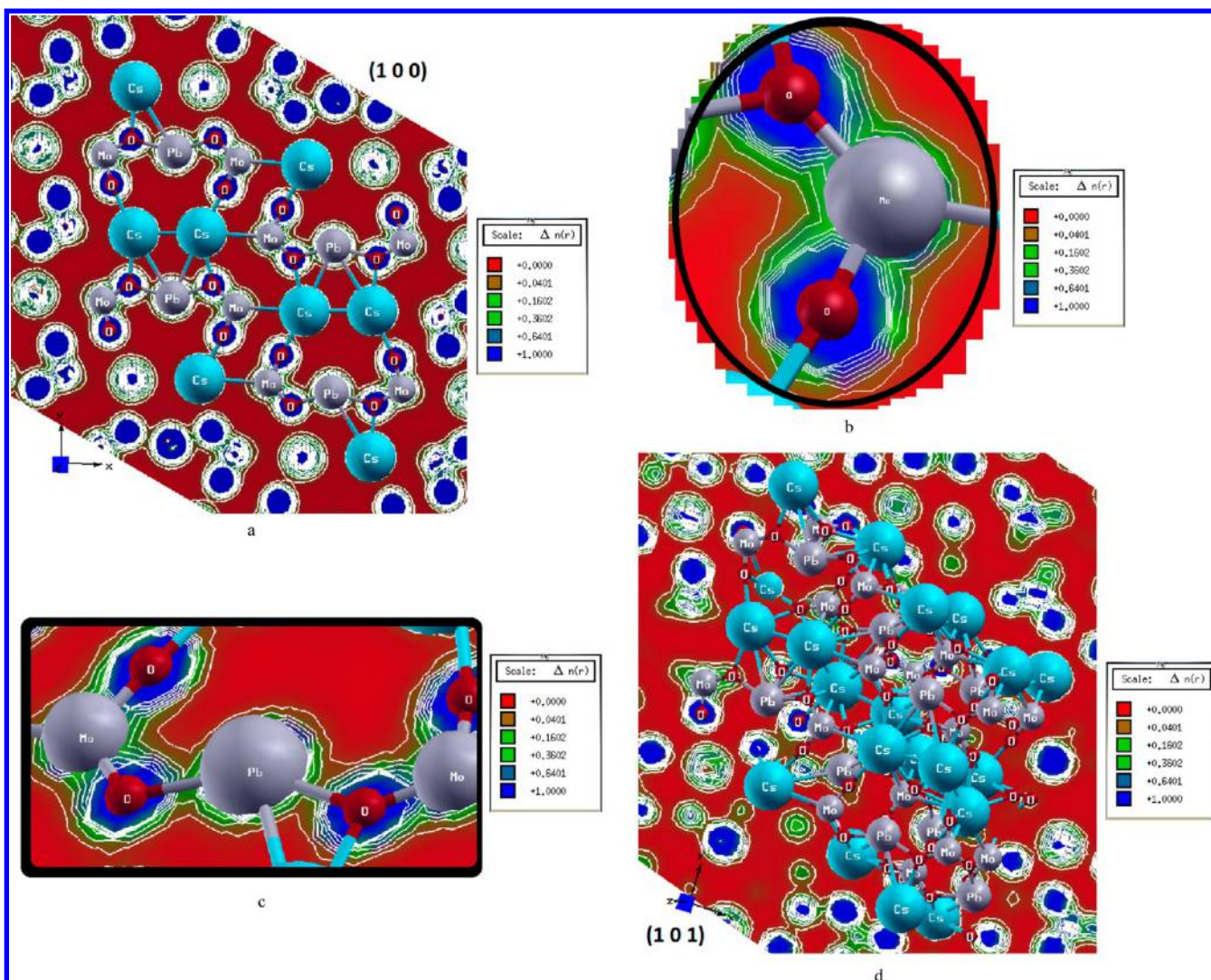
Figure 9. (a−d) Calculated electronic charge density distribution of α-Cs$_2$Pb(MoO$_4$)$_2$.

ferroelastic α-Pb$_3$(XO$_4$)$_2$ (X = P, V, As), where the main reasons are shifts of the lead atoms from the former 3-fold axes. These lead-containing palmierites along with α-K$_2$Pb(MoO$_4$)$_2$, α-A$_2$Pb-(WO$_4$)$_2$ (A = Cs, Rb), and many other compounds possessing distortive phase transitions from the trigonal palmierite-type phases to low-symmetry modifications are of considerable importance as a numerous group of compounds with ferroic properties. Aimed structure modification of double molybdates and other palmierite-related compounds (for example, with isomorphous substitutions) can be used to control their functional properties for possible applications as memory elements or switches.

The comparison of the XPS valence-band spectrum and the XES bands of α-Cs$_2$Pb(MoO$_4$)$_2$ on a common energy scale representing the energy distribution of the Mo 4d and O 2p states indicates that the Mo 4d and O 2p states contribute mainly to the central portion and at the valence band top, respectively, with significant contributions throughout the whole α-Cs$_2$Pb-(MoO$_4$)$_2$ valence-band region also. Our results indicate that the electronic structure of α-Cs$_2$Pb(MoO$_4$)$_2$ differs somewhat from the electronic structure of molybdates with general formula MMoO$_4$ (M = Mg, Ca, Ni, Zn, Cd, Ba, Pb, Sr) as well as of MWO$_4$ tungstates (M = Ca, Cu, Zn, Cr, Cd, Pb) in which the valence Mo(W) d and O p states contribute dominantly in the lower and upper portions of the valence band, respectively.

■ ASSOCIATED CONTENT

ⓢ Supporting Information

The Supporting Information is available free of charge on the ACS Publications website at DOI: 10.1021/acs.inorgchem.6b02653.

> (CIF)
>
> Optical image of α-Cs$_2$Pb(MoO$_4$)$_2$ microcrystals, TEM image of a typical Cs$_2$Pb(MoO$_4$)$_2$ particle, atom positions, equivalent isotropic heat parameters, and selected intera-tomic distances in α-Cs$_2$Pb(MoO$_4$)$_2$ structure (PDF)

■ AUTHOR INFORMATION

Corresponding Author

*Phone: +7 (383) 3308889. Fax: +7 (383) 3332771. E-mail: atuchin@isp.nsc.ru.

ORCID ⓘ

Victor V. Atuchin: 0000-0002-7424-5604

Denis P. Pishchur: 0000-0002-0532-6478

Pavel E. Plyusnin: 0000-0002-7494-6240

Ali H. Reshak: 0000-0001-9426-8363

Author Contributions

The manuscript was written through contributions of all authors.

Notes

■ REFERENCES

(1) Solodovnikov, S. F.; Klevtsova, R. F.; Klevtsov, P. V. A Correlation between the Structure and Some Physical Properties of Binary Molybdates (Tungstates) of Uni- and Bivalent Metals. *J. Struct. Chem.* **1994**, *35*, 879−889.

(2) Ra, H.-S.; Ok, K. M.; Halasyamani, P. S. Combining Second-Order Jahn-Teller Distorted Cations to Create Highly Efficient SHG Materials: Synthesis, Characterization, and NLO Properties of BaTeM$_2$O$_8$ (M = Mo^{6+} or W^{6+}). *J. Am. Chem. Soc.* **2003**, *125*, 7764−7765.

(3) Isupov, V. A. Ferroelectric and Ferroelastic Phase Transitions in Molybdates and Tungstates of Monovalent and Bivalent Elements. *Ferroelectrics* **2005**, *322*, 83−114.

(4) Solodovnikov, S. F.; Solodovnikova, Z. A.; Zolotova, E. S.; Yudanova, L. I.; Kardash, T. Yu.; Pavlyuk, A. A.; Nadolinny, V. A. Revised Phase Diagram of Li$_2$MoO$_4$-ZnMoO$_4$ System, Crystal Structure and Crystal Growth of Lithium Zinc Molybdate. *J. Solid State Chem.* **2009**, *182*, 1935−1943.

(5) Maczka, M.; Paraguassu, W.; Freire, P. T.; Majchrowski, A.; Pizani, P. S. Lattice Dynamics and Pressure-Induced Phase Transitions in α-BaTeMo$_2$O$_9$. *J. Phys.: Condens. Matter* **2013**, *25*, 125404.

(6) Shi, P. L.; Xia, Z. G.; Molokeev, M. S.; Atuchin, V. V. Crystal Chemistry and Luminescence Properties of Red-Emitting CsGd$_{1-x}$Eu$_x$(MoO$_4$)$_2$ Solid-Solution Phosphors. *Dalton Trans.* **2014**, *43*, 9669−9676.

(7) Tsyrenova, G. D.; Pavlova, E. T.; Solodovnikov, S. F.; Popova, N. N.; Kardash, T. Yu.; Stefanovich, S. Yu.; Gudkova, I. A.; Solodovnikova, Z. A.; Lazoryak, B. I. New Ferroelastic K$_2$Sr(MoO$_4$)$_2$: Synthesis, Phase Transitions, Crystal and Domain Structures, Ionic Conductivity. *J. Solid State Chem.* **2016**, *237*, 64−71.

(8) Lim, C. S.; Atuchin, V. V.; Aleksandrovsky, A. S.; Molokeev, M. S.; Oreshonkov, A. S. Incommensurately Modulated Structure and Spectroscopic Properties of CaGd$_2$(MoO$_4$)$_4$:Ho^{3+}/Yb^{3+} Phosphors for Up-Conversion Applications. *J. Alloys Compd.* **2017**, *695*, 737−746.

(9) Møller, C. K. The Structure of Pb(NH$_4$)(SO$_4$)$_2$ and Related Compounds. *Acta Chem. Scand.* **1954**, *8*, 81−87.

(10) Efremov, V. A.; Trunov, V. K. About Double Molybdates with Palmierite Type Structure. *Crystallogr. Rep.* **1974**, *19* (5), 989−993 (in Russian).

(11) Dudnik, E. F.; Kiosse, G. A. The Peculiarities of Atom Structure of Inorganic Ferroelastics. *Bull. Acad. Sci. USSR. Phys. Ser.* **1983**, *47*, 420−434 (in Russian).

(12) Trunov, V. K.; Efremov, V. A.; Velykodnyi, Yu. A. *Crystal Chemistry and Properties of Double Molybdates and Tungstates*; Nauka: Leningrad, 1986.

(13) Keppler, U. Die Struktur der Tieftemperaturform des Bleiphosphates, Pb$_3$(PO$_4$)$_2$. *Z. Kristallogr.* **1970**, *132*, 228−235.

(14) Guimaraes, D. M. C. Ferroelastic Transformations in Lead Orthophosphate and Its Structure as a Function of Temperature. *Acta Crystallogr., Sect. A: Cryst. Phys., Diffr., Theor. Gen. Crystallogr.* **1979**, *35*, 108−114.

(15) Dudnik, E. F.; Mnushkina, I. E. Domain Structure and Phase Transition in K$_2$Pb(MoO$_4$)$_2$ Single Crystals and Related Compounds. *Ukr. J. Phys.* **1977**, *22*, 1737−1738.

(16) Efremov, V. A.; Trunov, V. K. Distortion of the Palmierite Structure in K$_2$Pb(MoO$_4$)$_2$. *Dokl. Akad. Nauk SSSR* **1977**, *235*, 820−823.

(17) Gudkova, I. A.; Solodovnikova, Z. A.; Solodovnikov, S. F.; Zolotova, E. S.; Kuratieva, N. V. Phase Formation in Li$_2$MoO$_4$−Rb$_2$MoO$_4$−MMoO$_4$ (M = Ca, Sr, Ba, Pb) Systems and the Crystal Structure of α-Rb$_2$Pb(MoO$_4$)$_2$. *J. Struct. Chem.* **2011**, *52*, 1063−1069.

(18) Anderson, A. B.; Kim, Y.; Ewing, D. W.; Grasselli, R. K.; Tenhover, M. Electronic Properties of Bi$_2$O$_3$ and MoO$_3$ and Relationships to Oxidation Catalysis. *Surf. Sci.* **1983**, *134*, 237−256.

(19) Henrich, V. E.; Cox, P. A. *The Surface Science of Metal Oxides*; Cambridge University Press: Cambridge, 1994.

(20) Tokarz-Sobieraj, R.; Hermann, K.; Witko, M.; Blume, A.; Mestl, G.; Schlögl, R. Properties of Oxygen Sites at the MoO$_3$(010) Surface: Density Functional Theory Cluster Studies and Photoemission Experiments. *Surf. Sci.* **2001**, *489*, 107−125.

(21) Khyzhun, O. Y.; Strunskus, T.; Solonin, Y. M. XES, XPS and NEXAFS Studies of the Electronic Structure of Cubic MoO$_{1.9}$ and H$_{1.63}$MoO$_3$ Thick Films. *J. Alloys Compd.* **2004**, *366*, 54−60.

(22) Sayede, A. D.; Amriou, T.; Pernisek, M.; Khelifa, B.; Mathieu, C. An ab initio LAPW Study of the α and β Phases of Bulk Molybdenum Trioxide, MoO$_3$. *Chem. Phys.* **2005**, *316*, 72−82.

(23) Khyzhun, O. Y.; Bekenev, V. L.; Solonin, Y. M. Electronic Structure of Face-Centred Cubic MoO$_2$: A Comparative Study by the Full Potential Linearized Augmented Plane Wave Method, X-Ray Emission Spectroscopy and X-ray Photoelectron Spectroscopy. *J. Alloys Compd.* **2008**, *459*, 22−28.

(24) Rajagopal, S.; Nataraj, D.; Khyzhun, O. Y.; Yu; Djaoued, Y.; Robichaud, J.; Senthil, K.; Mangalaraj, D. Systematic Synthesis and Analysis of Change in Morphology, Electronic Structure and Photo-luminescence Properties of Pyrazine Intercalated MoO$_3$ Hybrid Nanostructures. *CrystEngComm* **2011**, *13*, 2358−2368.

(25) Bekenev, V. L.; Khyzhun, O. Y.; Atuchin, V. V. Electronic Structure of Monoclinic α-KY(WO$_4$)$_2$ Tungstate as Determined from First-Principles FP-LAPW Calculations and X-ray Spectroscopy Studies. *J. Alloys Compd.* **2009**, *485*, 51−58.

(26) Atuchin, V. V.; Aleksandrovsky, A. S.; Chimitova, O. D.; Diao, C.-P.; Gavrilova, T. A.; Kesler, V. G.; Krylov, A. S.; Bazarov, B. G.; Bazarova, J. G.; Lin, Z. S. Electronic Structure of β-RbSm(MoO$_4$)$_2$ and Chemical Bonding in Molybdates. *Dalton Trans.* **2015**, *44*, 1805−1815.

(27) Reshak, A. H. Microcrystalline β-RbNd(MoO$_4$)$_2$. *RSC Adv.* **2015**, *5*, 44960−44968.

(28) Atuchin, V. V.; Khyzhun, O. Y.; Chimitova, O. D.; Molokeev, M. S.; Gavrilova, T. A.; Bazarov, B. G.; Bazarova, J. G. Electronic Structure of β-RbNd(MoO$_4$)$_2$ by XPS and XES. *J. Phys. Chem. Solids* **2015**, *77*, 101−108.

(29) Kurtz, S. K.; Perry, T. T. A Powder Technique for the Evaluation of Nonlinear Optical Materials. *J. Appl. Phys.* **1968**, *39*, 3798−3813.

(30) Atuchin, V. V.; Gavrilova, T. A.; Gromilov, S. A.; Kostrovsky, V. G.; Pokrovsky, L. D.; Troitskaia, I. B.; Vemuri, R. S.; Carbajal-Franco, G.; Ramana, C. V. Low-Temperature Chemical Synthesis and

Microstructure Analysis of GeO_2 Crystals with α-quartz Structure. *Cryst. Growth Des.* **2009**, *9*, 1829−1832.

(31) Troitskaia, I. B.; Gavrilova, T. A.; Gromilov, S. A.; Sheglov, D. V.; Atuchin, V. V.; Vemuri, R. S.; Ramana, C. V. Growth and Structural Properties of α-MoO_3 (010) Microplates with Atomically Flat Surface. *Mater. Sci. Eng., B* **2010**, *174*, 159−163.

(32) Sheldrick, G. M. *SHELX97*, Release 97-2. University of Goettingen: Goettingen, Germany, 1997.

(33) Rajagopal, S.; Nataraj, D.; Khyzhun, O. Y.; Djaoued, Y.; Robichaud, J.; Kim, C.-K. Controlled Synthesis of MoO_3 Microcrystals by Subsequent Calcination of Hydrothermally Grown Pyrazine-MoO_3 Nanorod Hybrids and Their Photodecomposition Properties. *Mater. Chem. Phys.* **2013**, *141*, 383−392.

(34) Blaha, P.; Schwarz, K.; Madsen, G. K. H.; Kvasnicka, D.; Luitz, J. *WIEN2k, An augmented plane wave plus local orbitals program for calculating crystal properties*; Vienna University of Technology: Austria, 2001.

(35) Perdew, J. P.; Burke, K.; Ernzerhof, M. Generalized Gradient Approximation Made Simple. *Phys. Rev. Lett.* **1996**, *77*, 3865−3868.

(36) Tran, F.; Blaha, P. Accurate Band Gaps of Semiconductors and Insulators with a Semilocal Exchange-Correlation Potential. *Phys. Rev. Lett.* **2009**, *102*, 226401.

(37) Blöchl, P. E.; Jepsen, O.; Andersen, O. K. Improved Tetrahedron Method for Brillouin-Zone Integrations. *Phys. Rev. B: Condens. Matter Mater. Phys.* **1994**, *49*, 16223−16233.

(38) Belyaev, I. N.; Chikova, N. N. Systems of Chromates, Molybdates and Tungstates of Rubidium, Cesium and Lead. *Zh. Neorg. Khim.* **1964**, *9*, 2754−2760.

(39) Tsyrenova, G. D.; Bazarova, Z. G.; Mokhosoev, M. V. Double Molybdates of Cesium and Divalent Elements. *Dokl. Akad. Nauk USSR* **1987**, *294*, 387−389.

(40) In *Practical Surface Analysis*, 2nd ed.; Briggs, D., Seach, P. M., Ed.; John Wiley & Sons Ltd.: Chichester, 1990; Vol. *1* (Auger and X-Ray Photoelectron Spectroscopy).

(41) Khyzhun, O. Y.; Bekenev, V. L.; Atuchin, V. V.; Pokrovsky, L. D.; Shlegel, V. N.; Ivannikova, N. V. The Electronic Structure of Pb_2MoO_5: First-Principles DFT Calculations and X-ray Spectroscopy Measurements. *Mater. Des.* **2016**, *105*, 315−322.

(42) Bi, J. H.; Wu, L.; Zhang, Y. F.; Li, Z. H.; Li, J. Q.; Fu, X. Z. Solvothermal Preparation, Electronic Structure and Photocatalytic Properties of $PbMoO_4$ and $SrMoO_4$. *Appl. Catal., B* **2009**, *91*, 135−143.

(43) Sczancoski, J. C.; Cavalcante, L. S.; Marana, N. L.; da Silva, R. O.; Tranquilin, R. L.; Joya, M. R.; Pizani, P. S.; Varela, J. A.; Sambrano, J. R.; Siu Li, M.; Longo, E.; Andrés, J. Electronic Structure and Optical Properties of $BaMoO_4$ Powders. *Curr. Appl. Phys.* **2010**, *10*, 614−624.

(44) Matar, S. F.; Largeteau, A.; Demazeau, G. $AMoO_4$ (A = Mg, Ni) Molybdates: Phase Stabilities, Electronic Structures and Chemical Bonding Properties from First Principles. *Solid State Sci.* **2010**, *12*, 1779−1785.

(45) Cavalcante, L. S.; Moraes, E.; Almeida, M. A. P.; Dalmaschio, C. J.; Batista, N. C.; Varela, J. A.; Longo, E.; Siu Li, M. S.; Andrés, J.; Beltrán, A. A Combined Theoretical and Experimental Study of Electronic Structure and Optical Properties of β-$ZnMoO_4$ Microcrystals. *Polyhedron* **2013**, *54*, 13−25.

(46) Zhang, Y.; Holzwarth, N. A. W.; Williams, R. T. Electronic Band Structures of the Scheelite Materials $CaMoO_4$, $CaWO_4$, $PbMoO_4$, and $PbWO_4$. *Phys. Rev. B: Condens. Matter Mater. Phys.* **1998**, *57*, 12738−12750.

(47) Abraham, Y.; Holzwarth, N. A. W.; Williams, R. T. Electronic Structure and Optical Properties of $CdMoO_4$ and $CdWO_4$. *Phys. Rev. B: Condens. Matter Mater. Phys.* **2000**, *62*, 1733−1741.

(48) Khyzhun, O. Y.; Strunskus, T.; Cramm, S.; Solonin, Y. M. Electronic Structure of $CuWO_4$: XPS, XES and NEXAFS Studies. *J. Alloys Compd.* **2005**, *389*, 14−20.

(49) Khyzhun, O. Y.; Bekenev, V. L.; Solonin, Y. M. First-Principles Calculations and X-ray Spectroscopy Studies of the Electronic Structure of $CuWO_4$. *J. Alloys Compd.* **2009**, *480*, 184−189.

(50) Song, M.; Zhang, Q.; Liu, T.; Yin, J.; Guo, X.; Zhang, H.; Wang, X. First-Principles Study on Electronic States of $SrWO_4$ Crystals Containing F-Type Color Centers. *Curr. Appl. Phys.* **2009**, *9*, 812−815.

(51) Rajagopal, S.; Nataraj, D.; Khyzhun, O. Y.; Djaoued, Y.; Robichaud, J.; Mangalaraj, D. Hydrothermal Synthesis and Electronic Properties of $FeWO_4$ and $CoWO_4$ Nanostructures. *J. Alloys Compd.* **2010**, *493*, 340−345.

(52) Rajagopal, S.; Bekenev, V. L.; Nataraj, D.; Mangalaraj, D.; Khyzhun, O. Y. Electronic Structure of $FeWO_4$ and $CoWO_4$ Tungstates: First-Principles FP-LAPW Calculations and X-Ray Spectroscopy Studies. *J. Alloys Compd.* **2010**, *496*, 61−68.

(53) Zhou, X.; Liu, T.; Zhang, Q.; Cheng, F.; Qiao, H. Electronic Structure and Optical Properties of $CdWO_4$ with Oxygen Vacancy Studied from First Principles. *Solid State Commun.* **2010**, *150*, 5−8.

(54) Atuchin, V. V.; Troitskaia, I. B.; Khyzhun, O. Y.; Bekenev, V. L.; Solonin, Y. M. Electronic Structure of h-WO_3 and $CuWO_4$ Nanocrystals, Harvesting Materials for Renewable Energy Systems and Functional Devices. *Appl. Appl. Mech. Mater.* **2011**, *110*−*116*, 2188−2193.

(55) Khyzhun, O. Y.; Bekenev, V. L.; Atuchin, V. V.; Galashov, E. N.; Shlegel, V. N. Electronic Properties of $ZnWO_4$ Based on *ab initio* FP-LAPW Band-Structure Calculations and X-ray Spectroscopy Data. *Mater. Chem. Phys.* **2013**, *140*, 588−595.

(56) Menendez-Proupin, E.; Palacios, P.; Wahnon, P.; Conesa, J. C. Self-Consistent Relativistic Band Structure of the $CH_3NH_3PbI_3$ Perovskite. *Phys. Rev. B: Condens. Matter Mater. Phys.* **2014**, *90*, 045207.

(57) Even, J.; Pedesseau, L.; Jancu, J.-M.; Katan, C. Importance of Spin-Orbit Coupling in Hybrid Organic/Inorganic Perovskites for Photovoltaic Applications. *J. Phys. Chem. Lett.* **2013**, *4*, 2999−3005.